Review of Regularization Techniques in Electrocardiographic Imaging

Matija Milanič*, Vojko Jazbinšek** and Rok Hren**
*J. Stefan Institute, Ljubljana, Slovenia
**Institute of Mathematics, Physics and Mechanics, Ljubljana, Slovenia
Email: vojko.jazbinsek@imfm.si

***Abstract*—Regularization methodologies are an integral part in dealing with ill-posedness of inverse problem in electrocardiograhy, expressed in terms of potential distribution on the epicardium. In order to systematically evaluate various regularization techniques under controlled conditions, we employed progressively more complex idealized source models (from single dipole to triplet of dipoles) to calculate body surface potentials, which served as an input data to the inverse problem. In total, we examined, 13 different regularization techniques and found that non-quadratic methods (total variation algorithms) and first-order and second-order Tikhonov regularizations outperformed other methodologies.**

I. Introduction

It has been shown that there is an infinite number of internal electrical heart sources that can produce the same potential distribution on the body surface [1], [2]. Therefore, to solve such ill-posed inverse problem, an equivalent source model has to be presupposed. Some of the models, e.g., single dipole or single quadrupole, are rather crude approximations of the entire heart's electrical activity, while other models, e.g., epicardial potentials, can be actually measured. The inverse solution that employs the potential distribution on the epicardial surface as an equivalent source model or electrocardiographic imaging (ECGI) [3] has been widely studied in electrocardiography due to its inherent ill-posedness [4]–[7]. A plethora of regularization techniques have been applied to gauge wildly oscillating inverse solutions, however, there is a growing need to compare, structure, and unify those diversified regularization methods. In particular, such a comparison requires the use of the same volume conductor and the same cardiac source models in order to eliminate other sources of variation in results. In this study, we employed the same volume conductor model as in a related study [8] to systematically evaluate the performance of 13 different regularization techniques using progressively more complex idealized source models (from single dipole to triplet of dipoles).

II. Methods

A. Problem formulation

The equivalent potential distribution on the epicardial surface can be found from a known potential distribution on the torso surface - which can be in principle obtained using multichannel ECG devices [9] - by solving generalized Laplace's equation subjected to Cauchy boundary conditions [4]–[7]. Such a boundary-value problem must be in an arbitrarily shaped volume conductor approximated on a discretized solution domain as the system of linear equations. For the homogeneous and isotropic model of the human torso, this can be achieved by means of the boundary element method (BEM), which relates the potentials at the torso nodes (expressed as an m-dimensional vector Φ_{B}) to the potentials at the epicardial nodes (expressed as an n-dimensional vector Φ_{E})

$$\Phi_{\mathrm{B}} = \mathbf{A}\Phi_{\mathrm{E}} \tag{1}$$

where $\mathbf{A}$ is the transfer coefficient matrix ($m \times n$) and $n < m$. The transfer coefficient matrix depends entirely on the geometric integrands which can be calculated analytically [10], [11]. In principle, the epicardial potential distribution could be simply found in the form of a pseudo inverse; however, the matrix $\mathbf{A}$ is ill-conditioned, i.e., its singular values are limiting to zero with particular gap of separation in the singular value spectrum, which yields an unstable solution. A number of approaches have been developed to control the wild oscillations of the solution and the ones we have used and described in more details in the related study [8] are divided into three groups

1) Tikhonov regularizations: zero order (ZOT) [12], [13], first order (FOT) [7], [14] and second order (SOT) [13],
2) iterative techniques: truncated singular value decomposition [15] (zero order (ZTSVD), first order (FTSVD), and second order (STSVD)), conjugate gradient [16] (zero order (ZCG), first order (FCG), and second order (SCG)), ν-method (NU) [15], and MINRES method [16],
3) non-quadratic techniques [7], [17]: total variation (FTV), and total variation with Laplacian (STV).

We used geometry based on the torso shaped outer boundary, defined with m=771 nodes, and an internal, barrel-shaped cage with n=602 electrodes, which surrounded all sources (surrogate for the epicardial surface) [8].

B. Selection of sources

We created a cylindrical source space, consisted of 744 dipoles in 248 positions, which were arranged in 8 axial planes 10 mm apart along the polar z-axis, see Fig. 1. There were three perpendicular dipoles in each position: normal (radial, $\vec{p}_\rho$) and tangential (along the polar angle, $\vec{p}_\varphi$) to the cage side surface, and alongside the polar axis ($\vec{p}_z$). In the first and second source (axial) planes there were 7 source positions (Fig. 1c), one in the center and 6 arranged along a concentric circle with a radius of 10 mm (nodes of hexagon with side 10 mm). The center of the bottom plane was at (-16, 45, 230) mm in the Cartesian coordinate system of the torso-cage model. In the next two source planes (Fig. 1d), there were 19 positions on each plane, 7 as in the first and second planes and 12 arranged on an additional concentric circle with a radius of 20 mm (nodes of a dodecagon with side 10 mm). In the next two source planes, there were 37 positions on each plane (Fig. 1e), 19 as in the previous two planes, and 18 on an additional concentric circle with a radius of 30 mm (equivalent to the nodes of an octadecagon with a side length of 10 mm). In the last two source planes, there were 61 positions on each plane (Fig. 1f), 37 as in the previous two planes and 24 on an additional concentric circle with a radius of 40 mm (nodes of tetracosagon with sides of 10 mm).

From the above source space, we selected three different idealized source models:

1) single dipoles at 16 different locations and 3 different orientations (in total 48 combinations),
2) pairs of dipoles at 324 combinations, and
3) triplets of dipoles at 24 different combinations.

For single dipole source, we selected sources in four planes at levels (z_i in mm): bottom plane ($z_0 = 230$, Fig. 1c), two planes in the middle ($z_1 = 260$, Fig. 1d and $z_2 = 270$, Fig. 1e), and upper plane ($z_3 = 300$, Fig. 1f). On each plane, we selected four positions (in cylindrical coordinates ρ – radial distance, φ - polar angle, and z – height), one in the center (polar axis) and three on the outermost circle of a given plane (ρ_0=10, ρ_1=20, ρ_2=30, ρ_3=40 mm) at polar angles φ=-180°, -120° and -60°, see Figs. 2a–c.

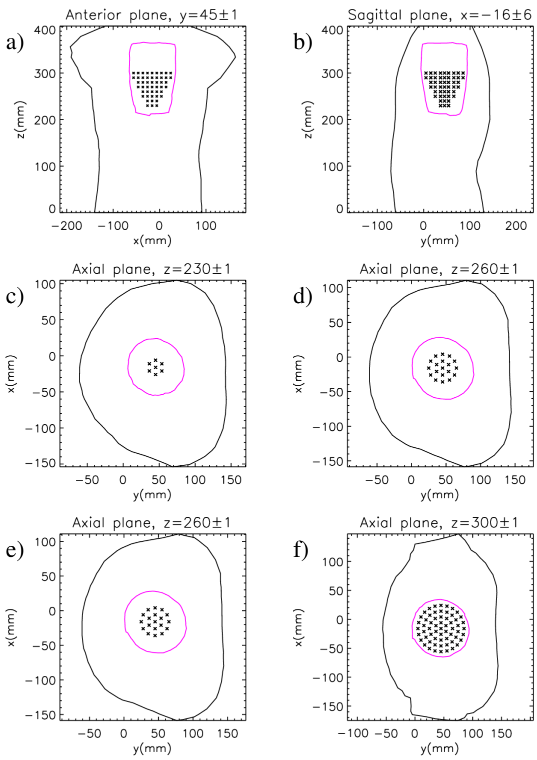

Fig. 1. Cross-sectional views of dipole positions denoted by a) Anterior, b) Sagittal and (c through f), Axial planes at different z levels. Torso and cage borders are displayed with black and magenta colors, respectively. On each plane, sources within x or y or z levels ± tolerance are displayed. The polar axis of the cylindrical cage is at x=-16 mm and y=45 mm.

For dual dipole sources, we selected single dipole sources in three planes at levels (z_i): two planes in the middle ($z_1 = 260$ and $z_2 = 270$), and in the upper plane ($z_3 = 300$), see Figs. 2d–f. Note, that we kept the same notation of planes as in the case of single dipole sources. On each plane, we selected only dipoles in the outermost circle with radial distances ρ_1, ρ_2 and ρ_3, respectively. We put the first single dipole on the right side (polar angle φ=-180°). The other dipoles are then positioned in angular steps of $\Delta\varphi_i$ in the anterior part

$$\varphi = -180^\circ + \Delta\varphi_i,\ -180^\circ + 2\Delta\varphi_i,\ \ldots, 0^\circ,$$

where $\Delta\varphi_1$=30°, $\Delta\varphi_2$=20° and $\Delta\varphi_3$=15°, with 6, 9 and 12 additional dipole positions in the three selected planes, respectively. We combined dipoles along the same direction (3 parallel $(\vec{p}_\rho, \vec{p}_\rho)$, $(\vec{p}_\varphi, \vec{p}_\varphi)$, $(\vec{p}_z, \vec{p}_z)$ and 3 anti-parallel $(\vec{p}_\rho, -\vec{p}_\rho)$, $(\vec{p}_\varphi, -\vec{p}_\varphi)$, $(\vec{p}_z, -\vec{p}_z)$ combinations), as well as dipoles 6 orthogonal combinations ($(\vec{p}_\rho, \vec{p}_\varphi)$, $(\vec{p}_\rho, \vec{p}_z)$, $(\vec{p}_\varphi, \vec{p}_\rho)$, $(\vec{p}_\varphi, \vec{p}_z)$, $(\vec{p}_z, \vec{p}_\rho)$, $(\vec{p}_z, \vec{p}_\varphi)$).

For 3-dipoles sources, we selected single dipole source positions that approximately form nodes of equilateral triangle. We formed six different triangles, which are named according to either an approximate cross-sectional plane where triangle nodes are positioned (Anterior and Sagittal) or a part of the cage (torso) where most nodes are positioned (Right) with added approximated distance between dipoles (side of a given triangle) in mm. We selected six triangles. The first node of Anterior–80 (Fig. 3a) and Sagittal–80 triangles is positioned in the center of the bottom plane ($z_0 = 230$).

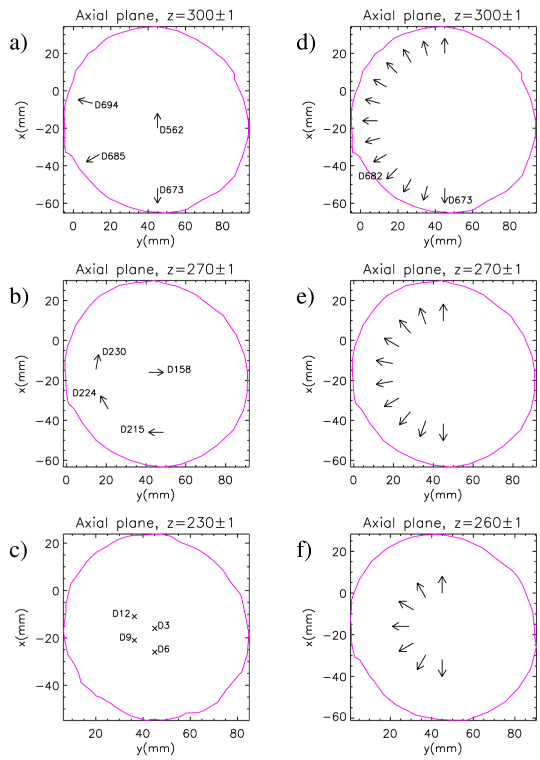

Fig. 2. Selected positions for single dipoles in different planes: a) z_3=300 mm (radial dipoles $\vec{p}_\rho$ are displayed), b) z_2=270 mm (dipoles along the polar angle $\vec{p}_\varphi$ are displayed) and c) z_2=260 mm (axial $\vec{p}_z$ dipoles are displayed). Labels denote dipole numbers in 744–dipoles source space (Fig. 1). Selected positions of dual dipole sources in planes: d) z_3=300 mm, e) z_2=270 mm and f) z_2=260 mm. Dipoles normal to the cage side ($\vec{p}_\rho$) surface are displayed.

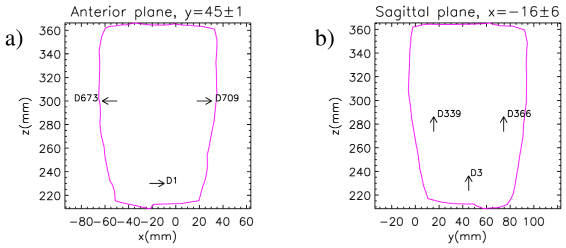

Fig. 3. Positions of triple dipole sources in a) Anterior–80 (radial $\vec{p}_\rho$ are displayed) and b) Sagittal–60 (axial $\vec{p}_z$ are displayed) triangles.

The other two nodes are positioned in the outermost circle (ρ_3=40 mm) of the upper source plane ($z_3 = 300$), with polar angles φ=(-180°, 0°) and (-90°,90°), respectively, see Fig. 3. Similar scheme was used also for constructing Anterior–60 and Sagittal–60 (Fig. 3b) triangles, where the other two nodes are positioned in the outermost circle (ρ=30 mm) of the source plane at z=280 mm. The first node of the Right–57 triangle is positioned in the center of the source plane at z=260 mm and the other two nodes are positioned in the outermost circle of the upper source plane at z_3, with polar angles φ=(-180°, -90°). The first node of the Right–42 triangle is positioned in the center of plane at z=250 mm and the other two nodes are positioned in the outermost circle of the source plane at z=280 mm, with polar angles φ=(-180°, -100°). For each triangle, we formed four 3-dipoles sources

1) normal with dipoles $(-\vec{p}_z, \vec{p}_\rho, \vec{p}_\rho)$
2) tangential with dipoles $(\vec{p}_\rho, -\vec{p}_z, \vec{p}_z)$
3) along the polar angle $(\vec{p}_\varphi, \vec{p}_\varphi, \vec{p}_\varphi)$, which are also all tangential to the cage side surface
4) axial with all dipoles along polar axis $(\vec{p}_z, \vec{p}_z, \vec{p}_z)$.

C. Data simulation and evaluation

For all selected single, dual and triple dipole sources, we simulated data at 602 leads of the cylindrical cage and at 771 nodes on the torso surface using boundary element method (BEM) [18]. In order to test the inverse solution, we added to the BEM calculated potential maps on a body (torso) surface 10 different random noise distributions at level (*S/N*=40 dB), where $S/N = 20\log_{10}\frac{\mathrm{RMS(signal)}}{\mathrm{RMS(noise)}}$. For each simulated data with added noise on the torso surface, we applied all 13 regularization techniques from section II-A to reconstruct the potential distribution on the cage surface. As a measure of reconstruction accuracy, we used the relative error (normalized RMS error) $\mathrm{RE} = ||\Phi_{\mathrm{E}}^{\mathrm{r}}\Phi_{\mathrm{E}}^{\mathrm{m}}||_2/||\Phi_{\mathrm{E}}^{\mathrm{m}}||_2$, and the correlation coefficient, $\mathrm{CC} = \Phi_{\mathrm{E}}^{\mathrm{r}}\cdot\Phi_{\mathrm{E}}^{\mathrm{m}}/||\Phi_{\mathrm{E}}^{\mathrm{r}}||_2||\Phi_{\mathrm{E}}^{\mathrm{m}}||_2$, where $\Phi_{\mathrm{E}}^{\mathrm{m}}$ are the directly-computed cylindrical-cage potentials and $\Phi_{\mathrm{E}}^{\mathrm{r}}$ are the reconstructed potentials. Since there are no specific clinical thresholds for RR and CC, we also compared qualitative features of both simulated and inversely computed potential maps, (e.g., areas of negative potentials and positions of extrema).

III. Results

Table I summarizes average reconstruction results for single, dual and triple dipole models with 40-dB input noise. Results show that NU and MINRES are the worst for all source configurations. Zero order methods (ZOT, ZCG, ZSTSVD) are also much worse than their first and second order equivalents (FOT, SOT, FTSVD, STSVD, FCG, SCG, FTV, STV), so we display results for those methods only in other tables. Best reconstruction results for all source configurations are on average obtained with FOT, SOT, FTV and STV methods. FTSTVD and STSVD methods have good performance only for single dipoles. FCG and SCG methods under-perform in reconstruction of dual dipoles.

TABLE I. Average $\overline{\mathrm{RE}}$±SD and $\overline{\mathrm{CC}}$*

Method	Single dipoles $\overline{\mathrm{RE}}$±SD	Single dipoles $\overline{\mathrm{CC}}$	Dual dipoles $\overline{\mathrm{RE}}$±SD	Dual dipoles $\overline{\mathrm{CC}}$	Triple dipoles $\overline{\mathrm{RE}}$±SD	Triple dipoles $\overline{\mathrm{CC}}$
ZOT	0.42±0.11	0.90	0.50±0.13	0.85	0.49±0.12	0.86
FOT	0.28±0.16	0.95	0.43±0.17	0.88	0.40±0.20	0.89
SOT	0.36±0.12	0.94	0.43±0.14	0.89	0.42±0.13	0.90
ZTSVD	0.46±0.13	0.89	0.53±0.14	0.83	0.51±0.13	0.85
FTSVD	0.29±0.17	0.94	0.46±0.19	0.86	0.48±0.22	0.87
STSVD	0.31±0.20	0.92	0.48±0.21	0.84	0.45±0.23	0.85
ZCG	0.42±0.12	0.90	0.52±0.14	0.84	0.50±0.12	0.86
FCG	0.31±0.18	0.93	0.48±0.19	0.85	0.42±0.20	0.88
SCG	0.30±0.15	0.94	0.44±0.18	0.87	0.39±0.17	0.90
NU	0.59±0.15	0.78	0.65±0.15	0.73	0.65±0.17	0.72
MINRES	0.44±0.14	0.88	0.56±0.17	0.80	0.53±0.12	0.84
FTV	0.29±0.16	0.94	0.42±0.16	0.89	0.40±0.18	0.90
STV	0.28±0.15	0.94	0.42±0.17	0.89	0.39±0.18	0.90

*Averaged over all selected groups of dipole sources

TABLE II. Single dipoles in different directions

Method	radial $\vec{p}_\rho$ $\overline{\mathrm{RE}}$±SD	radial $\vec{p}_\rho$ $\overline{\mathrm{CC}}$	polar angle $\vec{p}_\varphi$ $\overline{\mathrm{RE}}$±SD	polar angle $\vec{p}_\varphi$ $\overline{\mathrm{CC}}$	polar axis $\vec{p}_z$ $\overline{\mathrm{RE}}$±SD	polar axis $\vec{p}_z$ $\overline{\mathrm{CC}}$
FOT	0.27±0.16	0.95	0.30±0.18	0.93	0.26±0.15	0.95
SOT	0.32±0.10	0.94	0.35±0.13	0.92	0.30±0.11	0.95
FTSVD	0.29±0.17	0.94	0.31±0.19	0.93	0.27±0.16	0.95
STSVD	0.31±0.20	0.93	0.33±0.22	0.91	0.29±0.20	0.93
FCG	0.31±0.18	0.93	0.33±0.19	0.92	0.29±0.17	0.94
SCG	0.29±0.16	0.94	0.33±0.16	0.93	0.27±0.15	0.95
FTV	0.29±0.11	0.97	0.33±0.19	0.92	0.30±0.16	0.94
STV	0.28±0.13	0.96	0.31±0.18	0.93	0.26±0.15	0.95

TABLE III. Single dipoles in different planes

Method	z_0=230 mm $\overline{\mathrm{RE}}$	z_0=230 mm $\overline{\mathrm{CC}}$	z_1=260 mm $\overline{\mathrm{RE}}$	z_1=260 mm $\overline{\mathrm{CC}}$	z_2=270 mm $\overline{\mathrm{RE}}$	z_2=270 mm $\overline{\mathrm{CC}}$	z_3=300 mm $\overline{\mathrm{RE}}$	z_3=300 mm $\overline{\mathrm{CC}}$
FOT	0.25	0.97	0.17	0.98	0.27	0.95	0.41	0.88
SOT	0.31	0.95	0.24	0.98	0.29	0.95	0.44	0.86
FTSVD	0.26	0.97	0.17	0.98	0.29	0.95	0.44	0.86
STSVD	0.27	0.96	0.17	0.98	0.30	0.94	0.51	0.81
FCG	0.28	0.96	0.18	0.98	0.31	0.94	0.47	0.84
SCG	0.26	0.96	0.18	0.98	0.28	0.95	0.49	0.87
FTV	0.30	0.95	0.20	0.97	0.28	0.95	0.38	0.89
STV	0.29	0.96	0.17	0.98	0.26	0.96	0.38	0.90

Table II displays results for single dipoles in different directions. Results show that dipoles oriented along the polar angle (tangential to the cage surface) are slightly worse than results for dipoles oriented along the polar axis and for radial dipoles (normal to the cage surface). Table III displays results for single dipoles in different planes. Results show that the quality of reconstruction depends on a distance of sources from the cage surface. The best results are obtained for the plane z_1, where the selected dipoles on the outer circle are ∼27 mm from the side surface. The worst results are obtained for the plane z_3 where the selected dipoles are ∼10 mm from the side surface. The selected dipoles on the plane z_2 are ∼18 mm from the side surface. The selected dipoles on the bottom

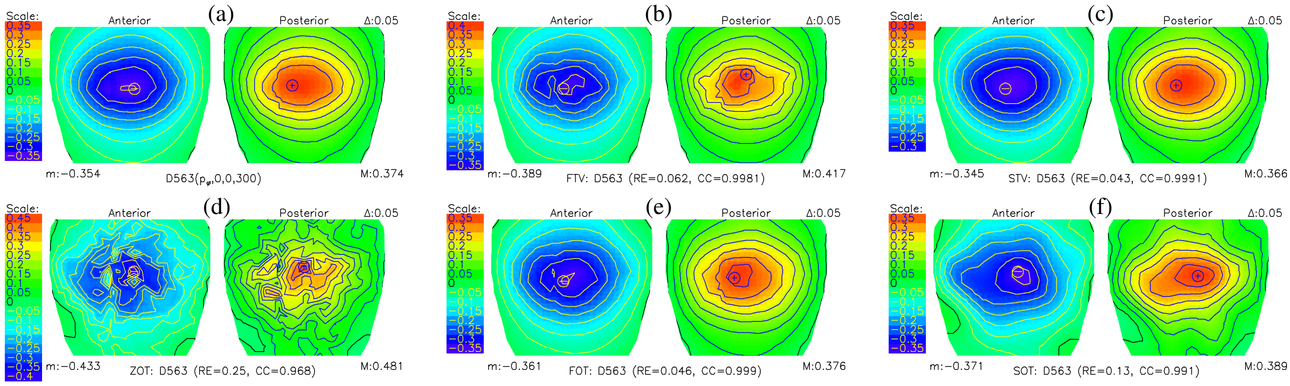

Fig. 4. a) Cage potential distribution due to single dipole positioned in the center axial plane z_3=300 mm, oriented towards the anterior side of the torso. D563(p_φ,0,0,300) bellow the map denotes dipole number in the 744-dipole source space from Fig. 1, dipole orientation and coordinates in cylindrical coordinate system, respectively. Note, that this dipole is located in the same position as the dipole D562 in Fig. 2a. "M" denotes maximum potential, "m" denotes minimum and Δ step between iso-potential lines potential for a given map, respectively. Inversely computed cage potentials using b) FTV and c) STV (first and second order total variation algorithm), d) ZOT, e) FOT and f) SOT (zero, first and second order Tikhonov regularization methods. Below each reconstruction map, RE and CC values are displayed. Each map is displayed on the anterior and posterior cage side, where vertical direction corresponds to cage height in the range $z \in [218, 360]$ mm, and horizontal direction corresponds to polar angle multiplied with the cage radius at a given height (note, that in Figs. 1-3 torso and cage cross-sections in the zx, zy and xy planes are shown).

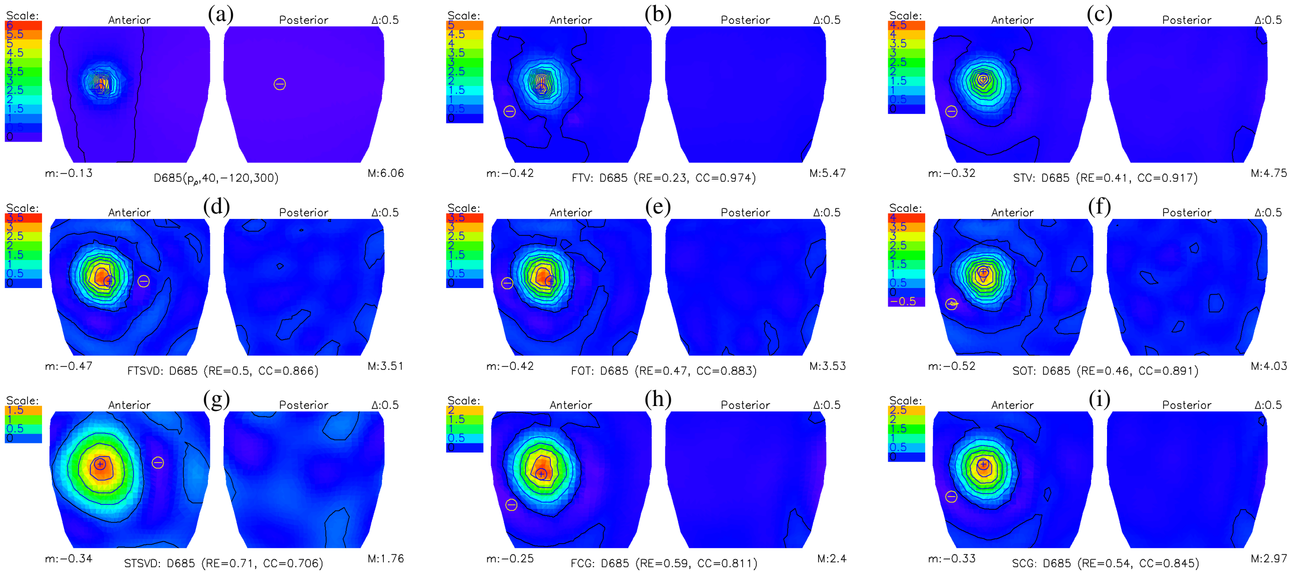

Fig. 5. a) Cage potential distribution due to single dipole positioned closed to the cage surface (ρ=400 mm, φ=-120°, dipole D685 in Fig. 2a) in the axial plane z_3=300 mm, oriented towards the cage surface (p_ρ). Inversely computed cage potentials using b) FTV, c) STV, d) FTSVD, e) FOT, f) SOT, g) STSVD h) FCG and i) SCG.

plane z_0 are ~33 mm from the side surface, but they are only ~18 mm from the cage bottom surface.

Fig. 4 compares directly simulated cage potentials with inversely computed potentials using ZOT, FOT, SOT, FTV, and STV, for a single dipole source near the cage center. Isopotential map forms a nice symmetrical dipolar pattern distributed over the whole cage surface in this case. Results clearly shows that ZOT performs worse than FOT and SOT, similar conclusion can be reached for other zero-order methods (ZTSVD and ZCG) as well as for MINRES and NU methods. The lowest/highest values of RE/CC were obtained with STV and FOT methods.

Fig. 5 compares directly simulated cage potentials with inversely computed potentials using FTV, STV, FOT, SOT, FTSVD, STSVD, FCG, and ZCG, for a single dipole source near and oriented normal to the cage edge. In this case, isopotential map has non-zero values in a rather small region, while FTV method clearly outperforms other methods.

Table IV displays results for dual dipoles in different planes. Like in the case of single dipoles (Table III), the quality of reconstruction depends on a distance of sources from the cage surface. Table V displays results for different orientations of dual dipoles. It seems that dual dipole orientations have no effect on the quality of reconstructed results, the anti-parallel orientations gives

TABLE IV. DUAL DIPOLES IN DIFFERENT PLANES

Method	z_1=260 mm		z_2=270 mm		z_3=300 mm	
	RE±SD	CC	RE±SD	CC	RE±SD	CC
FOT	0.21±0.081	0.97	0.36±0.09	0.93	0.59±0.08	0.80
SOT	0.29±0.055	0.96	0.37±0.08	0.93	0.56±0.09	0.82
FTSVD	0.23±0.090	0.97	0.39±0.12	0.91	0.62±0.11	0.77
STSVD	0.27±0.093	0.97	0.40±0.12	0.90	0.67±0.10	0.73
FCG	0.23±0.080	0.97	0.41±0.09	0.91	0.66±0.08	0.75
SCG	0.22±0.095	0.97	0.37±0.10	0.92	0.61±0.08	0.79
FTV	0.24±0.092	0.96	0.37±0.11	0.92	0.54±0.13	0.83
STV	0.22±0.083	0.97	0.36±0.10	0.93	0.56±0.10	0.82

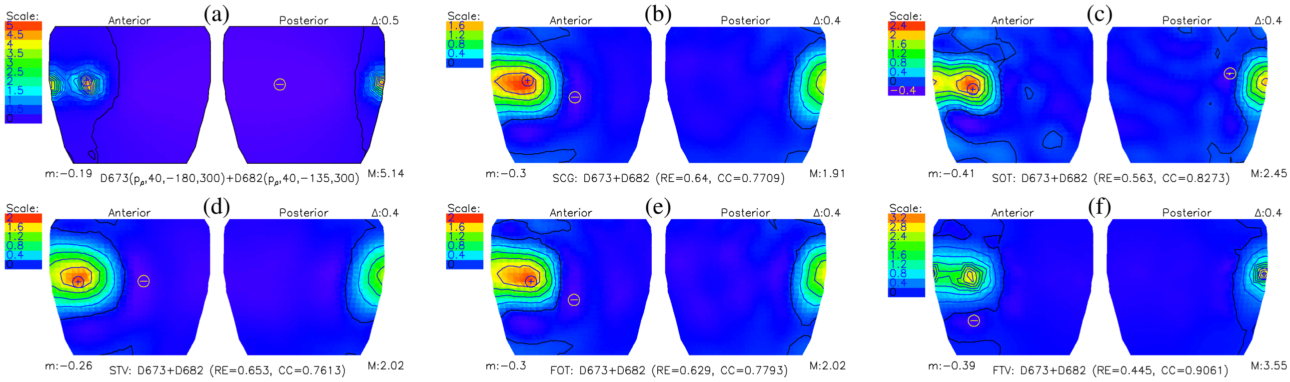

Fig. 6. a) Cage potential distribution due to a pair of parallel dipoles, 30.6 mm apart, positioned close to the surface of the cage in the axial plaen $z_3 = 300$ mm (dipoles D673 and D682 in Fig. 2d). Inversely computed cage potentials using b) SCG, c) SOT, d) STV, e) FOT, and f) FTV.

TABLE V. DIFFERENT ORIENTATIONS OF DUAL DIPOLES

Method	parallel		orthogonal		anti-parallel	
	RE±SD	CC	RE±SD	CC	RE±SD	CC
FOT	0.40±0.16	0.90	0.42±0.17	0.89	0.47±0.18	0.85
SOT	0.41±0.12	0.90	0.43±0.12	0.89	0.47±0.18	0.86
FTSVD	0.43±0.18	0.88	0.44±0.18	0.87	0.52±0.22	0.81
STSVD	0.46±0.21	0.85	0.46±0.21	0.85	0.53±0.22	0.80
FCG	0.46±0.18	0.87	0.47±0.18	0.86	0.52±0.21	0.82
SCG	0.42±0.16	0.89	0.43±0.17	0.88	0.49±0.21	0.84
FTV	0.39±0.14	0.91	0.41±0.14	0.90	0.46±0.21	0.85
STV	0.40±0.15	0.90	0.41±0.16	0.90	0.46±0.20	0.86

TABLE VI. DIFFERENT GROUPS OF TRIPLE DIPOLES

Method	Anterior-60		Right-42		Sagittal-60	
	RE±SD	CC	RE±SD	CC	RE±SD	CC
FOT	0.43±0.23	0.86	0.08±0.02	0.99	0.30±0.05	0.95
SOT	0.38±0.06	0.92	0.25±0.08	0.96	0.35±0.04	0.94
FTSVD	0.42±0.22	0.87	0.11±0.02	0.99	0.35±0.11	0.93
STSVD	0.41±0.19	0.90	0.09±0.02	0.99	0.34±0.07	0.94
FCG	0.37±0.08	0.93	0.09±0.03	0.99	0.32±0.06	0.95
SCG	0.34±0.08	0.94	0.13±0.05	0.99	0.29±0.04	0.95
FTV	0.38±0.14	0.92	0.10±0.02	0.99	0.34±0.11	0.93
STV	0.37±0.07	0.93	0.08±0.03	0.99	0.32±0.05	0.95

Method	Anterior-80		Right-57		Sagittal-80	
	RE±SD	CC	RE±SD	CC	RE±SD	CC
FOT	0.60±0.09	0.80	0.54±0.06	0.84	0.46±0.05	0.89
SOT	0.57±0.09	0.81	0.53±0.04	0.85	0.45±0.05	0.89
FTSVD	0.62±0.14	0.77	0.60±0.13	0.78	0.52±0.13	0.84
STSVD	0.63±0.11	0.76	0.64±0.13	0.75	0.60±0.13	0.79
FCG	0.62±0.08	0.77	0.58±0.07	0.81	0.52±0.07	0.85
SCG	0.58±0.08	0.81	0.54±0.07	0.84	0.48±0.06	0.88
FTV	0.57±0.13	0.81	0.54±0.10	0.83	0.44±0.08	0.90
STV	0.59±0.10	0.80	0.52±0.05	0.85	0.44±0.06	0.89

TABLE VII. DIFFERENT ORIENTATIONS OF TRIPLE DIPOLES

Method	normal $-\vec{p}_z,\vec{p}_\rho,\vec{p}_\rho$		axial $\vec{p}_z,\vec{p}_z,\vec{p}_z$		tangential $\vec{p}_\rho,-\vec{p}_z,\vec{p}_z$		tangential $\vec{p}_\varphi,\vec{p}_\varphi,\vec{p}_\varphi$	
	RE	CC	RE	CC	RE	CC	RE	CC
FOT	0.42	0.89	0.33	0.93	0.50	0.82	0.35	0.92
SOT	0.43	0.89	0.42	0.90	0.45	0.88	0.39	0.92
FTSVD	0.49	0.83	0.34	0.92	0.55	0.79	0.37	0.92
STSVD	0.50	0.82	0.37	0.91	0.54	0.80	0.40	0.89
FCG	0.46	0.86	0.35	0.92	0.48	0.85	0.39	0.90
SCG	0.42	0.88	0.34	0.93	0.45	0.87	0.36	0.92
FTV	0.31	0.95	0.35	0.92	0.51	0.83	0.42	0.89
STV	0.39	0.90	0.35	0.92	0.46	0.87	0.35	0.92

on average only slightly worse results than parallel and orthogonal orientations. The same conclusion is also valid for different combinations of parallel, anti-parallel and orthogonal dual dipoles.

Fig. 6 compares directly simulated cylindrical-cage potentials with inversely computed potentials using SCG, SOT, STV, FOT, and FTV, when the two dipoles were 30.6 mm apart. It is evident that two distinct extrema were reconstructed only when using SOT (relative error of 0.56) or FTV (0.44); it is interesting that for this specific example, the Laplacian was a more suitable operator than the gradient when applying Tikhonov regularization, while the opposite was true for the total variation technique. When taking averages, however, the difference among regularization techniques in the reconstruction of two-dipole potential distributions on the cylindrical-cage surface was small and results were nearly identical when using, FOT (0.43±0.17), SOT (0.43±0.14), FTV (0.42±0.17), or STV (0.42±0.17). These observations point toward the often-neglected notion that qualitative features of reconstructed maps may show different comparative assessment than do quantitative summary statistics (e.g., relative error), and that in some instances, smaller relative errors may not mean more potent qualitative discrimination of localized events.

Table VI displays results for different groups of triple dipoles. Like in the case of single dipoles (Table III) and dual (Table IV), the quality of reconstruction depends on a distance of sources from the cage surface. The worst results are for Anterior–80 and Sagittal–80 triangles, where all nodes are close to the cage surface. On the other hand, we got almost prefect results for triple dipoles on nodes of Right-42 triangle, which are all quite deep inside the cage. Dipoles in this configuration are also relatively close to each other (∼42 mm), so they are not likely to generate a complex potential distribution on the cage surface.

Table VII displays results for different orientations of triple dipoles. The worst results are obtained for tangential ($\vec{p}_\rho,-\vec{p}_z,\vec{p}_z$) orientation. Fig. 7 shows results for a such triple dipole source in Anterior–80 (Fig. 3a). It is interesting to note, that all reconstructed maps have similar pattern for all presented methods, but none can focus 3 dipole sources: one on the bottom source plane (z_0), which is not clearly seen in this view of BEM calculated map (Fig. 7a), and the other two on the left

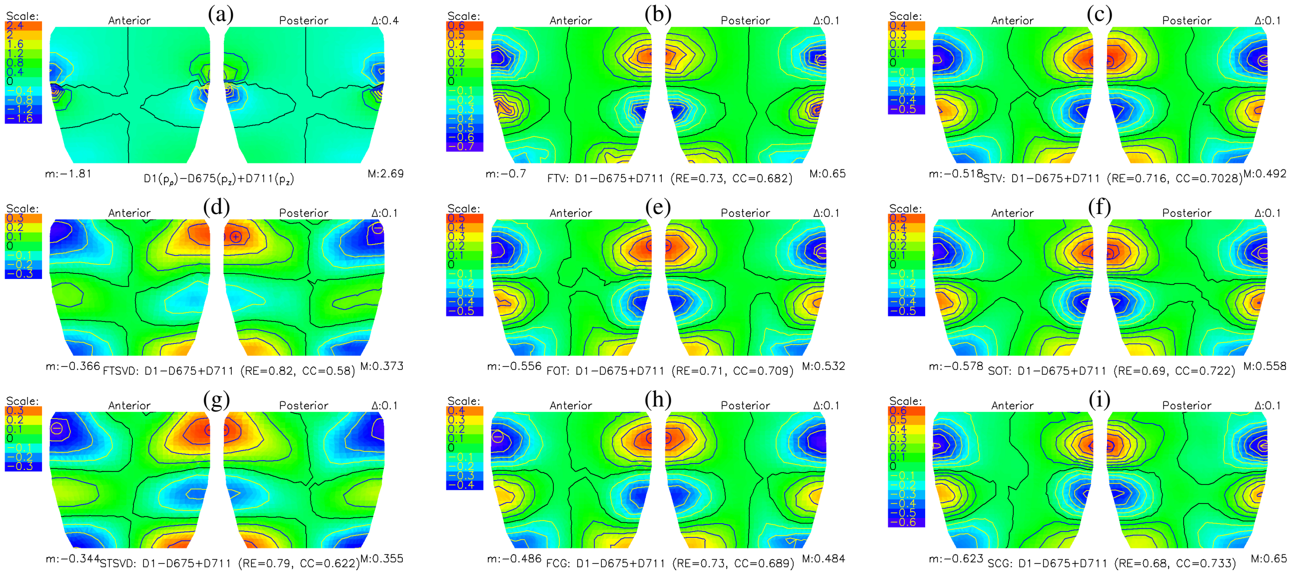

Fig. 7. a) Cage potential distribution due to triple dipoles in Anterior–80 triangle positioned closed and oriented tangentially ($\vec{p}_\rho, -\vec{p}_z, \vec{p}_z$) to the cage surface. Inversely computed cage potentials using b) FTV, c) STV, d) FTSVD, e) FOT, f) SOT, g) STSVD h) FCG and i) SCG.

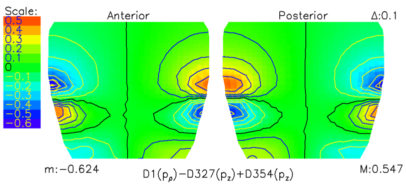

Fig. 8. Cage potential distribution due to triple dipoles in Anterior–60 triangle oriented tangentially ($\vec{p}_\rho, -\vec{p}_z, \vec{p}_z$) to the cage surface.

and right side of the upper source plane(z_3). However, one can clearly deduce from reconstructed maps the presence of 3 dipoles, but a bit deeper because the dipolar patterns are more spread. In fact, these reconstructed maps look more related to the corresponding source in Anterior–60 triangle, where dipoles are closer to each other (60 instead of 80 mm) and are not so close to the cage surface, see Fig. 8.

IV. Conclusions

The main finding of our study is that - for idealized source models - non-quadratic methods (total variation algorithms) and first-order and second-order Tikhonov regularizations outperformed other regularization methodologies. This study is a necessary step in comprehensive validation of various regularization methodologies by comparing them systematically and under controlled conditions.

References

[1] E. Frank, "Spread of current involume conductors of finite extent," *Ann. N. Y. Acad. Sci.*, vol. 65, pp. 980–1002, 1957.

[2] D. B. Geselowitz, "Dipole theory in electrocardiography," *Am. J. Cardiol.*, vol. 14, pp. 301–306, 1964.

[3] R. L. Lux, "Electrocardiographic mapping. noninvasive electrophysiological cardiac imaging," *Circulation*, vol. 87, pp. 1040–1042, 1993.

[4] H. Oster, B. Taccardi, R. L. Lux, P. R. Ershler, and Y. Rudy, "Noninvasive electrocardiographic imaging: reconstruction of epicardial potentials, electrograms, and isochrones and localization of single and multiple cardiac events," *Circulation*, vol. 96, pp. 1012–24, 1997.

[5] Y. Rudy and B. J. Messinger-Rapport, "The inverse problem in electrocardiography: Solutions in terms of epicardial," *Crit. Rev. Biomed. Eng.*, vol. 16, pp. 215–268, 1988.

[6] R. Hren, G. Stroink, and B. M. Horáček, "Accuracy of single-dipole inverse solution when localising ventricular pre-excitation sites: simulation study," *Med. Biol. Eng. Comp.*, vol. 36, pp. 323–329, 1998.

[7] P. Colli-Franzone, E. Macchi, and C. Viganotti, "Oblique dipole layer potentials applied to electrocardiology," *Ann. Biomed. Eng.*, vol. 37, pp. 902–912, 2009.

[8] M. Milanič, V. Jazbinšek, R. S. MacLeod, D. H. Brooks, and R. Hren, "Assessment of regularization techniques for electrocardiographic imaging problem," *J. Electrocardiol.*, vol. 47, pp. 20–28, 2014.

[9] R. Trobec, "Computer analysis of multichannel ecg," *Comput. Biol. Med.*, vol. 33, pp. 215–226, 2003.

[10] J. de Munck, "A linear discretization of the volume conductor boundary integral equation using analytically integrated elements," *IEEE Trans. Biomed. Eng.*, vol. BME–39, pp. 986–990, 1992.

[11] A. Ferguson, X. Zhang, and G. Stroink, "A complete linear discretization for calculating the magnetic field using the boundary element method," *IEEE Trans. Biomed. Eng.*, vol. 41, pp. 455–60, 1994.

[12] A. Tikhonov and V. Arsenin, *Solutions of Ill-Posed Problems*. Washington, DC: Winston, 1997.

[13] D. H. Brooks, G. F. Ahmad, R. D. MacLeod, and G. M. Maratos, "Inverse electrocardiography by simultaneous imposition of multiple constraints," *IEEE Trans. Biomed. Eng.*, vol. BME–46, pp. 3–18, 1999.

[14] P. Colli-Franzone, B. Taccardi, and C. Viganotti, "An approach to inverse calculation of epicardial potentials from body surface maps," *Adv. Cardiol.*, vol. 21, pp. 50–54, 1978.

[15] P. C. Hansen, *Rank-Deficient and Discrete Ill-Posed Problems*. Philadelphia, PA: SIAM, 1998.

[16] M. Hanke, *Conjugate Gradient Type Methods for Ill-Posed Problems*. Harlow: Longman Scientific & Technical, 1995.

[17] R. S. M. D. H. Brooks, K. G. Srinidhi and D. R. Kaeli, "Multiply constrained cardiac electrical imaging methods," in *Subsurface Sensors and Applications*, C. Nguyen, Ed., vol. 3752. Piscataway, NJ: Proc SPIE, 1999, pp. 1770–1771.

[18] A. Barnard, I. Duck, M. Lynn, and W. Timlake, "The application of electromagnetic theory to electrocardiography," *Biophys.J.*, vol. 7, pp. 443–491, 1967.